A Palladium-Based MOF for the Preferential Sorption of Benzene

Kevin Dedecker, Martin Drobek, V. Rouessac, Anne Julbe

To cite this version:

Kevin Dedecker, Martin Drobek, V. Rouessac, Anne Julbe. A Palladium-Based MOF for the Preferential Sorption of Benzene. ACS Applied Materials & Interfaces, 2023, 15 (5), pp.6831-6838. 10.1021/acsami.2c20034 . hal-04065751

HAL Id: hal-04065751

https://hal.umontpellier.fr/hal-04065751v1

Submitted on 4 May 2023

A Palladium-based MOF for the Preferential Sorption of Benzene

Kevin Dedecker, Martin Drobek, Vincent Rouessac, Anne Julbe*

Institut Européen des Membranes (IEM); CNRS, ENSCM, Univ Montpellier; Place Eugène Bataillon; 34095 Montpellier; France

KEYWORDS: Metal Organic Framework, Palladium, sorption, benzene, aromatics, volatile organic compounds, Quartz Crystal Microbalance

Abstract

The selective sorption of volatile aromatic compounds is a challenging issue for their total abatement. Despite the well-known affinity of palladium toward rich π systems, the studies dedicated to VOC capture with Pd(II) based-MOFs are still very scarce. Intending to shed more light on this complex topic, this work compares the adsorption properties of two isostructural MOFs $[Cu(2\text{-pymo})_2]_n$ and $[Pd(2\text{-pymo})_2]_n$, and their selectivity for the sorption of linear, cyclic or aromatic VOCs. The combination of both experimental and computational investigations highlights an increasing aromatic affinity over saturated hydrocarbons when palladium is chosen as metal center ($n_{Benzene}/n_{n\text{-hexane}}= 1.8$ at 0.5 p/p_0) in the MOF framework instead of copper ($n_{Benzene}/n_{n\text{-hexane}}= 0.7$ at 0.5 p/p_0). Furthermore, $[Pd(2\text{-pymo})_2]_n$ clearly exhibits a preferential adsorption of benzene over toluene ($n_{Benzene}/n_{Toluene}= 1.7$ at 0.5 p/p_0), due to the steric hindrance effects of the latter. The present results clearly underline the attractiveness of Pd-based MOFs for the design of selective aromatic adsorbents. Moreover, they also highlight the $[Pd(2\text{-pymo})_2]_n$ MOF as a relevant candidate for the selective capture of benzene, by a synergistic combination of both charge interactions and steric hindrance effects.

Introduction

Unprecedented environmental threats resulting from human activities are altering the planet with climate change, ozone depletion, deforestation, water scarcity, and increasing pollution of water and air. The growing emission of volatile organic compounds (VOCs) strongly contributes to the deterioration of the environment[1–3] and jeopardizes the integrity of living beings[4–6]. Amongst the organic pollutants classified as VOCs, a particular attention is given to aromatic compounds such as benzene and its derivatives[7], due to their deleterious effects on human health. These compounds are mainly generated by industrial emissions (e.g. petrochemical processes and derived products such as crude oil, petrol, glues, paints, furniture wax, and detergents) but also by tobacco smoke, gas stations, and motor vehicle exhausts. Benzene is notoriously responsible for a wide range of diseases including leukemia and anemia[8,9]. It is considered officially as a human carcinogen and the tolerated personal exposure limit is continuously decreasing (100 ppm in 1927, 1 ppm in 2000)[10]. Despite a significant effort to reduce their emission, the presence of volatile aromatic compounds is hardly avoidable in urban areas. Moreover, it turns out that indoor exposure to benzene pollution may reach 1.5 times the outdoor street level due to its continuous accumulation in confined spaces[11]. One of the considered options to preserve individuals from the noxious effects of these pollutants bears on an effective reduction/monitoring of the daily exposure by employing specifically designed materials for their capture and/or detection[12]. In this area, the application of activated carbons, zeolites and silica is largely discussed in the literature. However, these materials suffer from either a lack of selectivity (adsorption of a wide range of VOCs) and/or a low adsorption capacity[13]. Despite their low cost, it may be difficult to overcome these aforementioned limitations. Hence, it makes sense to explore the potential of other relevant materials with greater chemical versatility.

Metal-Organic Frameworks (MOFs) are hybrid materials which are well known for their rich structural diversity, the versatility of their properties, and their attractive sorption performance. They are composed of inorganic bricks connected through organic ligands to form highly porous structures[14] which can be advantageously tuned at the nanoscale to fit properly the requirements of each selected application. For instance, the spacer length adjustment allows to tailor the unit cell dimensions which control both the molecular sieving effect[15] and host-guest interactions by confining guest molecules[16]. Furthermore, the affinity to specific adsorbates can be enhanced by a judicious functionalization of ligands[17]. It must be underlined that metal centers may also significantly affect host-guest interactions either by the presence of open metal sites or by a specific affinity of the metal for the target adsorbate(s). As an example, the investigation of the CPO-27 series (Ni, Co, Mg, Cu and Zn) for the desulfurization of fuel[18] evidenced that CPO-27(Ni) offers the highest affinity toward thiophene due to strong nickel-sulfur interactions.

Amongst different transition metals, palladium holds a special place due to its ability to interact strongly with hydrogen[19] and with conjugated molecules such as alkenes[20], alkynes[21], and aromatics[22] *via* π-complexation mechanism. Hence, palladium is a significant asset to boost the sorption selectivity of porous materials for this series of molecules. It has been proven that the incorporation of palladium species (e.g. Pd atoms or nanoparticles, salts, oxides or complexes) within materials is able to catalyze reactions[23], contribute to H_2 sorption, dissociation, and spillover[24–26], enhance sensor sensitivity[27] and promote VOCs capture[28].

Despite the appealing potentialities of palladium-based materials, only few MOFs with Pd as a metal node were reported in the literature. This is mainly due to their tedious synthesis which often requires post-synthetic modification strategies to circumvent the formation of undesired by-products obtained in one pot synthesis (e.g. isolated PdO or amorphous materials)[29–32]. In order to clearly assess the potential of Pd-MOFs for the abatement of aromatic vapors, especially the benzene removal, the present work reports a comparative study of two isostructural MOFs referred as $[Cu(2\text{-pymo})_2]_n$[33] and $[Pd(2\text{-pymo})_2]_n$[32] (2-pymo = 2-pyrimidinolate) exposed to four model VOC compounds: n-hexane (linear alkane), cyclohexane (cyclic alkane), benzene and toluene (aromatics). Experimental isotherms obtained by QCM (Quartz Crystal Microbalance) measurements were combined with computational adsorption results in a comprehensive study in order to highlight the role of palladium nodes for the selective sorption/capture of aromatics.

Experimental section

Materials and methods

All reagents were purchased from commercial suppliers and used without any further purification. The structure and purity of the synthesized materials were verified by Powder X-Ray Diffraction (PXRD), N_2 adsorption-desorption measurements, thermogravimetric analysis (TGA), and Fourier-Transformed infrared (FTIR) spectroscopy. The powder diffraction patterns of crystalline materials were recorded by using PANanalytical X'Pert Pro diffractometer (Ni-filtered Cu-Kα radiation, 40 kV, 20 mA) from 5 to 50° (2θ). N_2 adsorption-desorption isotherms were measured at 77 K (liquid nitrogen bath) using Micromeritics ASAP 2020 equipment. Samples were outgassed for 12 h at 130°C under vacuum. Thermogravimetric analyses were carried out with TA instruments SDT 2960 under dry air at a constant heating rate of 5°C/min from 25 to 600°C. FTIR spectra were recorded from 500 to 4000 cm^{-1} (resolution of 4 cm^{-1}) with Nicolet Nexus FT-IR apparatus in reflection mode. Vapor adsorption isotherms were recorded with a Quartz Crystal Microbalance (QCM). The QCM setup is composed of a quartz resonator (AT-cut quartz, 14 mm, 6 MHz) working with a Maxtek TM-400 controller and 0.5 L chamber with injected VOC vapors[34]. The pumping system (Alcatel Drytel 1025), with membrane and turbomolecular pumps, reached pressured below 10^{-1} Pa for both purge and complete desorption.

Synthesis of $[Pd(2\text{-}pymo)_2]_n$ and $[Cu(2\text{-}pymo)_2]_n$

The MOF synthesis protocols reported in literature were followed with only slight modifications and the final materials were analyzed to identify the products and check their purity. $[Pd(2\text{-}pymo)_2]_n$ was obtained in two steps: synthesis of $[PdCl_2(2\text{-}Hpymo)_2]$ followed by its base-promoted polymerization to $[Pd(2\text{-}pymo)_2]_n$[30,32]. In more detail, a fresh Na_2PdCl_4 solution was prepared by dissolving $PdCl_2$ (0.6 mmol) in a NaCl solution (1.2 mmol in 10 mL of distillated water) under stirring and left for 12h. $[PdCl_2(2\text{-}Hpymo)_2]$ was synthesized by dissolving 2-Hpymo (1.2 mmol) in the freshly prepared Na_2PdCl_4 solution, for 4h at room temperature. The resulting solid was then filtered out and washed with water. The preparation of $[Pd(2\text{-}pymo)_2]_n$ was carried out by refluxing a solution containing $[PdCl_2(2\text{-}Hpymo)_2]$ (0.4 mmol) and KOH (0.4 mmol) dissolved in 10 mL of distillated water for 20h. The product was filtered out and washed with water, yielding a yellow crystalline powder. $[Cu(2\text{-}pymo)_2]_n$ was produced by mixing $CuCl_2.2H_2O$ (1.0 mmol) and 2-Hpymo (2.0 mmol) in 30 mL of

NH_4OH solution ($[NH_3]\approx25\%$) and stirring at room temperature for 48h[33]. The purple solid was then recovered by centrifugation and washed with water.

VOC sorption measurements using QCM

For each MOF material, VOC adsorption isotherms were recorded with QCM set-up equipped with quartz crystals (6MHz, purchased from Neyco) whose surface was covered with the selected MOF powder. Samples were prepared by depositing few drops of a suspension containing 2 mg of the MOF powder in 1 mL of methanol. The coated quartz crystals were then dried at 120°C for 2h. The deposited mass of MOF was estimated by the difference of frequencies measured by QCM before and after deposition, using the Sauerbrey equation[35]. Before any measurement, the chamber was pumped down to limit vacuum ~10^{-3} mbar in order to desorb MOF. Partial pressure was varied from 0 to 0.9 p/p_0 for all four VOCs (n-hexane, cyclohexane, benzene, and toluene). The quartz holder was kept at 25°C during the whole data collection to get the mass uptake isotherm of the sorbed VOC within the MOF.

Computational Methods

Computational methods were used to determine the theoretical microstructural characteristics of solvent-free $[Pd(2\text{-pymo})_2]_n$, $[Cu(2\text{-pymo})_2]_n$ (rhombohedral) and $[Cu(2\text{-pymo})_2]_n$ (cubic) structures. The surface area (SA) and pore volume (V_p) were estimated using RASPA software[36]. The average occupation profile of all studied adsorbates in the MOF networks (density plot) was depicted through Grand Canonical Monte Carlo (GCMC) simulation. System sizes were selected by considering the Van der Walls cutoff (12Å) and supercells were created with lengths larger than at least twice the cutoff value. More precisely, 2x2x1 and 2x2x2 supercells for $[Cu(2\text{-pymo})_2]_n$ and $[Pd(2\text{-pymo})_2]_n$ were considered, respectively. Uncharged United-Atom TraPPE (TraPPE-UA) model[37,38] was used for n-hexane while benzene was modeled with Explicit-Atom TraPPE (TraPPE-EA) model[39,40]. Concerning MOF structures, their atoms were taken as single Lennard-Jones sites whose parameters were extracted concomitantly from UFF[41] and Dreiding[42] force fields. The atomic charge assignment was ensured by the use of the classical "charge equilibration" method. Interactions between MOF structures and hydrocarbon molecules were described by a Lennard-Jones potential using Lorentz-Berthelot mixing rules. The Ewald sum technique was used to compute electrostatic interactions. The simulation was composed of 1,000,000 Monte Carlo steps for equilibration and 1,000 steps for production and the temperature was set at 25°C.

Results and discussion

Description of the MOF structures

The $[Pd(2\text{-pymo})_2]_n$ framework results from the polymerization of $[PdCl_2(2\text{-Hpymo})_2]$ in alkaline medium. The latter is a square-planar complex composed of one Pd(II) atom connected to two chloride atoms and two 2-Hpymo ligands through nitrogen atoms. This Pd-N bond ensuring the connection between the metal and the ligand remains within the resulting MOF structure. The polymerization leads to the formation of a 3D microporous sodalite-type network **(Figure 1)**. $[Cu(2\text{-pymo})_2]_n$ adopts the same topology and thus can be considered as its isoreticular form. Strictly speaking, its structure consists of sodalitic β cages ($Ø_{pore} \approx 9$ Å) connected through four- and six-membered ring windows denoted 4MR and 6MR, respectively **(Table 1)**. One may distinguish two types of 6MR windows: *i)* smaller and hydrophilic one decorated by carbonyl groups ($6MR_{\_CO}$) and *ii)* larger and hydrophobic one surrounded by C-H groups ($6MR_{\_H}$). Hence, one may consider both MOFs as amphiphilic due to the presence of pores with antagonist water adsorption behaviors. Furthermore, $[Cu(2\text{-pymo})_2]_n$ exhibits higher flexibility in comparison to its $[Pd(2\text{-pymo})_2]_n$ analog. Indeed, upon hydration, $[Cu(2\text{-pymo})_2]_n$ undergoes phase transition from cubic to rhombohedral structure[33]. In order to complete the comparison between both structures and discuss their accessibility for the transport of the molecular species considered in this work, the size of pore apertures has been estimated from their crystallographic structures **(Table 1)**. One may notice that the size of $6MR_{\_CO}$ pore aperture is larger for $[Cu(2\text{-pymo})_2]_n$ than for its analog whatever the phase, while only the rhombohedral phase exhibits larger 6MR_H pore apertures.

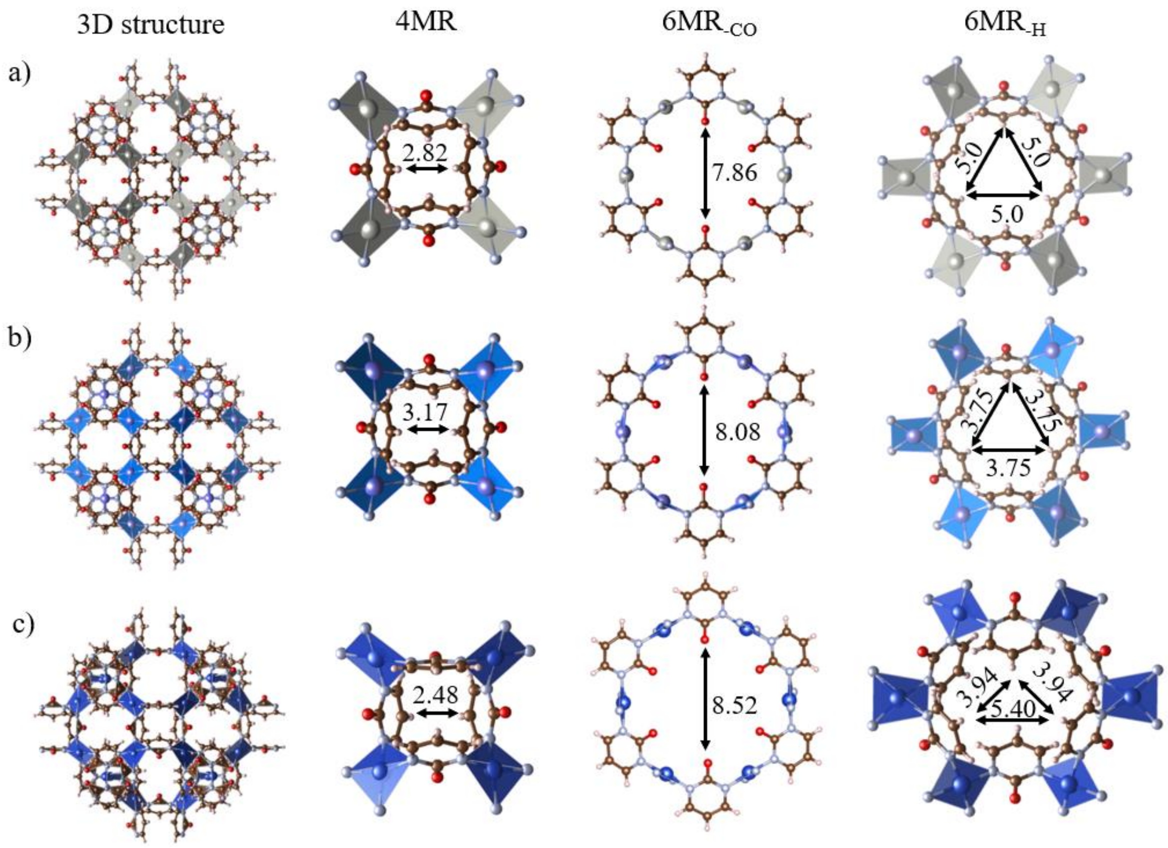

Figure 1. Structural description of a) [Pd(2-pymo)$_2$]$_n$, b) [Cu(2-pymo)$_2$]$_n$ (cubic) and c) [Cu(2-pymo)$_2$]$_n$ (rhombohedral). The general 3D structure is given with the three types of windows (4MR: 4 membered-ring; 6MR: 6 membered-ring). The pore aperture size is noted in Å. Color: grey (palladium), blue (copper), brown (carbon), white (hydrogen), pale blue (nitrogen), and red (oxygen).

Table 1. Measured values of pore apertures, theoretical surface area, and pore volume for [Pd(2-pymo)$_2$]$_n$ and [Cu(2-pymo)$_2$]$_n$.

	Phase	4MR (Å)	6MR$_{\_CO}$ (Å)	6MR$_{\_H}$ (Å)	SA (m²/g)	V$_p$ (cm³/g)
[Pd(2-pymo)$_2$]$_n$	Cubic	2.82	7.86	5.00/5.00/5.00	694	0.27
[Cu(2-pymo)$_2$]$_n$	Cubic	3.17	8.08	3.75/3.75/3.75	571	0.21
[Cu(2-pymo)$_2$]$_n$	Rhombohedral	2.48	8.52	5.40/3.94/3.94	406	0.16

Synthesis and characterization of MOFs

XRD patterns of the synthesized materials allowed to identify the crystalline phases and assess their purity **(Figure 2)**. The diffraction pattern of the synthesized [Cu(2-pymo)$_2$]$_n$ sample corresponds to the rhombohedral phase while [Pd(2-pymo)$_2$]$_n$ features a cubic phase. Interestingly, both MOFs seem to preserve their structural integrity when stored in air for one month **(Figure S1)**, although [Cu(2-pymo)$_2$]$_n$ shows slight changes in the width and intensity of the diffraction lines. This might be attributed to the higher flexibility of the Cu-based structure in comparison with its Pd-analog. Therefore, adsorbed water (air moisture) within cavities can interact with the structure and induce slight rotation of ligands, thus affecting intereticular distances. FTIR spectra do not exhibit any band corresponding to the free ligand, thus confirming the complete removal of unreacted chemicals **(Figure 3)**. Nevertheless, the broad band at 3500 cm^{-1} is attributed to the presence of water molecules remaining within the MOF cavities. Overall, similar absorption spectra were obtained for both materials, essentially caused by their isostructural character. N_2 adsorption-desorption isotherms were measured on outgassed samples (130°C under vacuum) and the BET method was applied to determine the experimental specific surface area **(Figure S2)**. For both MOFs, the measured surface areas fit values reported in literature (373 vs 350 m^2/g[33] and 705 vs 600 m^2/g[30,32] for [Cu(2-pymo)$_2$]$_n$ and [Pd(2-pymo)$_2$]$_n$, respectively), although being slightly higher, possibly caused by the reduced amount of defects, PdO and/or better cleaning. Interestingly, these experimental values also fit theoretical ones obtained by simulation (373 vs 406 and 705 vs 694 m^2/g for [Cu(2-pymo)$_2$]$_n$ and [Pd(2-pymo)$_2$]$_n$, respectively. This observation tends to indicate that the MOF activation treatment (outgassing) was efficient as pores are free of any adsorbed species. Thermogravimetric analysis of both MOFs was operated up to 600°C with a gradual temperature increase of 5°C/min under air flow **(Figure S3)**. The TGA profile of [Cu(2-pymo)$_2$]$_n$ encompasses three steps. A first dehydration occurs when water vapor is released from the structure between 30 and 110°C. Lately, a second dehydration step takes place up to 250°C after which the structure collapses slowly and decomposes completely above 500°C. Note that a similar TGA profile was reported for HKUST-1 (copper based-MOF containing open metal sites), and the second desorption step corresponded to the release of water molecules strongly coordinated to copper sites[43,44]. However, unlike HKUST-1, both [Cu(2-pymo)$_2$]$_n$ and [Pd(2-pymo)$_2$]$_n$ do not contain open metal sites. Therefore, in the present case, one may assume that residual water is still present after the first dehydration step due to strong interactions between Cu^{2+} sites and water molecules. Regarding [Pd(2-pymo)$_2$]$_n$, the TGA curve exhibits two main steps including desorption of water molecules up to 110°C followed by the structure collapse starting already at 330°C. The absence of the second dehydration step reveals weaker interactions between palladium sites and water, thus resulting in different adsorption behavior compared to its copper based-analog.

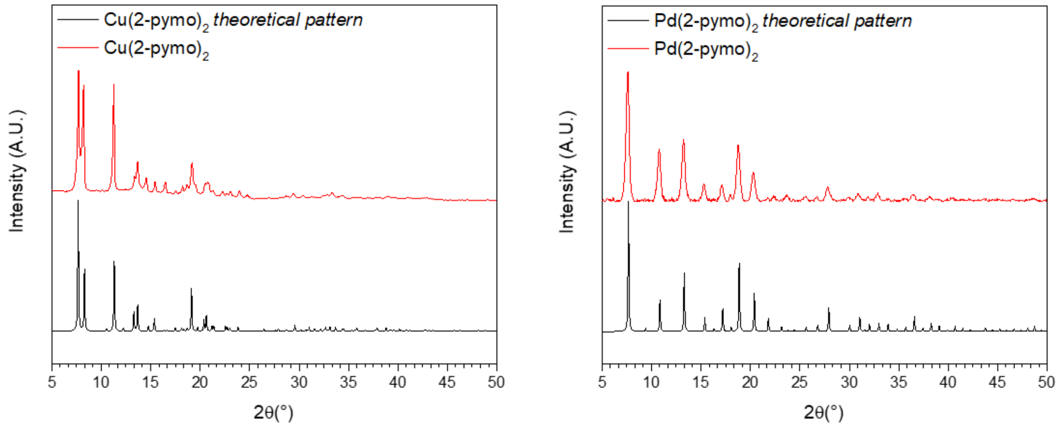

Figure 2. Comparison of experimental XRD patterns of the synthesized MOF powders (red) with the simulated XRD patterns (black).

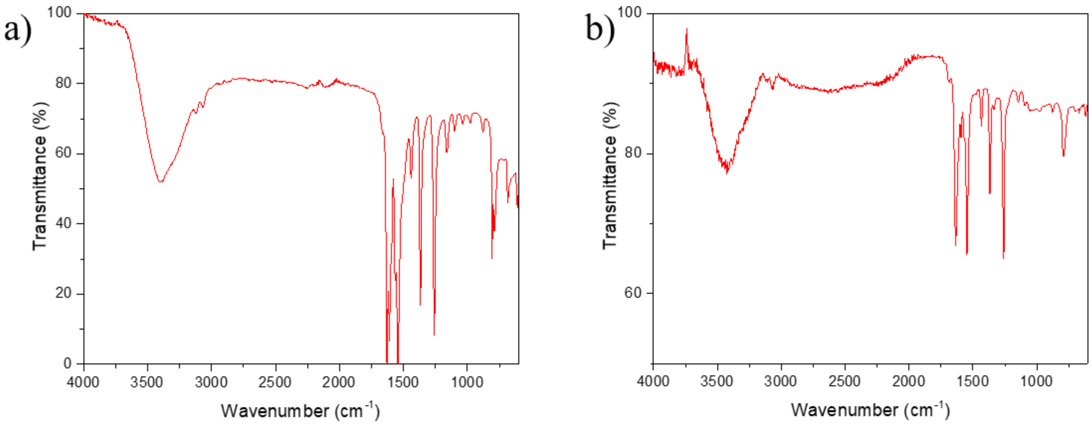

Figure 3. FTIR spectra of a) $[Cu(2\text{-}pymo)_2]_n$ and b) $[Pd(2\text{-}pymo)_2]_n$.

Adsorption of VOCs

Both $[Pd(2\text{-}pymo)_2]_n$ and $[Cu(2\text{-}pymo)_2]_n$ were exposed to four VOC vapors cited in **Table 2**. As mentioned before, $[Cu(2\text{-}pymo)_2]_n$ may exhibit cubic or rhombohedral phase depending on the presence of potential guests molecules in its porous structure. Therefore, the PXRD patterns of this material exposed to the selected VOCs **(Figure 4)** were recorded in order to identify the phase to be considered afterward. The presence of rhombohedral phase was confirmed for both compounds.

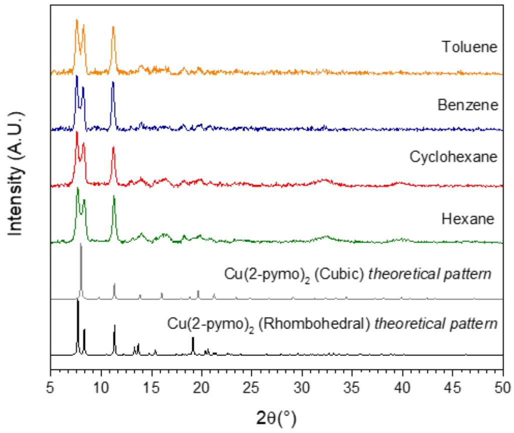

Figure 4. PXRD patterns of [Cu(2-pymo)$_2$]$_n$ exposed to VOCs.

Adsorption isotherms derived from QCM show an increase of adsorbed amount at $p/p_0<0.2$ followed by a monotonous slight loading. More specifically for [Cu(2-pymo)$_2$]$_n$, the VOC uptake can be ranked as follows: n-hexane > benzene >> toluene ≈ cyclohexane **(Figure 5.a)**. This trend is consistent with literature findings regarding hydrocarbon selectivity toward apolar type-MOFs. Pirngruber et al.[45] showed that MOFs exhibiting apolar character such as ZIF-8, tend to adsorb alkanes over alkenes or aromatics, while ionic MOFs such as CPO-27 (cationic) or RHO-ZMOF (anionic), tend to favor conjugated molecules over alkanes. Concerning [Cu(2-pymo)$_2$]$_n$, different factors can explain its sorption selectivity ($n_{Benzene}/n_{n\text{-}hexane}= 0.7$ at 0.5 p/p_0) **(Figure S4)**. The high loading of n-hexane is attributed concomitantly to its smaller kinetic diameter (4.3 Å) and higher flexibility which enhance its diffusion within the structure and thus allow its accommodation efficiently within pores. In contrast, the adsorbed amount of toluene is the lowest in the series, in part due to its larger kinetic diameter (5.8 Å) and its more rigid structure. However, despite their similar kinetic diameters, benzene and toluene clearly differ in their adsorbed amounts. This phenomenon might be explained by the particularity of aromatic molecules to organize themselves through π interactions (e.g. π-π stacking)[46]. Indeed, packing configurations of benzene and toluene strongly differ due to the steric hindrance generated by the -CH_3 group in toluene[47,48]. The higher content of adsorbed benzene compared to toluene results most likely from better pore filling caused by higher packing in MOF cages.

Some differences are noticed when comparing adsorption isotherms of both isostructural MOFs. The trend observed for $[Pd(2\text{-pymo})_2]_n$ shows deviations from its Cu-based analog and the VOC adsorption preferences can be ranked as follows: benzene >> cyclohexane > toluene > n-hexane **(Figure 5.b)**. As expected, benzene is clearly the dominant adsorbate within the series. Interestingly, n-hexane and cyclohexane loadings are lower but very similar, indicating a potential weaker affinity of these molecules toward $[Pd(2\text{-pymo})_2]_n$ ($n_{Benzene}/n_{n\text{-hexane}}$= 1.8 at 0.5 p/p_0) **(Figure S4)**, reaching typically the absorption capacity of benzene ~0.42 $mol_{Benzene}/mol_{[Pd(2\text{-pymo})2]n}$. This hypothesis is reinforced by the differences in adsorption enthalpies for benzene and cyclohexane onto $PdCl_2$ ($\Delta H_{benzene}$: 39-46 kJ/mol, $\Delta H_{cyclohexane}$: 21-29 kJ/mol)[22]. The lower affinity of cyclohexane can be clearly explained by the lack of π-electrons in the molecule. Similar to $[Cu(2\text{-pymo})_2]_n$, benzene and toluene do not adsorb in the same manner in $[Pd(2\text{-pymo})_2]_n$ ($n_{Benzene}/n_{Toluene}$= 1.7 at 0.5 p/p_0) **(Figure S4)**. Such difference could again result from steric effect, limiting accommodation of toluene molecules in the MOF porous structure and their access to palladium sites. Therefore, one may conclude that the affinity of $[Pd(2\text{-pymo})_2]_n$ is unambiguously turned to aromatics but more importantly, this particular structure displays significant preference for benzene over toluene. First assumptions might be proposed regarding the benzene sorption mechanisms within $[Pd(2\text{-pymo})_2]_n$. We may hypothesize that first, benzene chemisorption occurs at low pressures due to the strong interactions with Pd nodes. Then at higher pressure physisorption may be invoked, involving π-π interactions between the "free" and the already chemisorbed benzene molecules. The results indicate that the difference of adsorption uptake is strongly affected by three main characteristics of the VOC molecule: kinetic diameter, flexibility/rigidity and presence/absence of π electrons.

It should be highlighted that the overall lower adsorption capacity of $[Pd(2\text{-pymo})_2]_n$ compared to $[Cu(2\text{-pymo})_2]_n$ is counterbalanced by its remarkably high selectivity for benzene in the tested VOC series. This is particularly noticeable when comparing the adsorption isotherms per mole of adsorbent **(Figure S4)** but also when VOCs are considered as liquid (in mL) accommodated within the MOF porous structure **(Figure S5)**. This finding emphasizes the interest of $[Pd(2\text{-pymo})_2]_n$ as a preferential benzene sorbent applicable for its favored removal or sensing. In comparison, the Cu-based analog can be used for the simple capture of a broad spectrum of hydrocarbon molecules when no selectivity is required. It is also noteworthy to realize that the high atomic mass of Pd (106.4 g.mol^{-1}) compared to Cu (63.5 g.mol^{-1}) contributes to lower the apparent adsorption capacity of [Pd(2-pymo)$_2$]$_n$ measured in mmol$_{adsorbate}$/g$_{MOF}$. Hence, for a given volume of sorbent, the adsorption capacities of Pd and Cu-based MOFs are more comparable, and [Pd(2-pymo)$_2$]$_n$ appears as a competitive material for the design of devices for the specific capture or detection of benzene.

Table 2. List of adsorbates, characteristics and kinetic diameters.

Adsorbate	Type	Shape	Flexibility	Kinetic diameter (Å)	Saturation vapor pressure at 25°C (mbar)
n-hexane	Alkane	Linear	Flexible	4.3	199.4
Cyclohexane	Alkane	Cyclic	Flexible	6.0	130.7
Benzene	Aromatics	Cyclic	Rigid	5.8	126.9
Toluene	Aromatics	Cyclic	Rigid	5.8	37.1

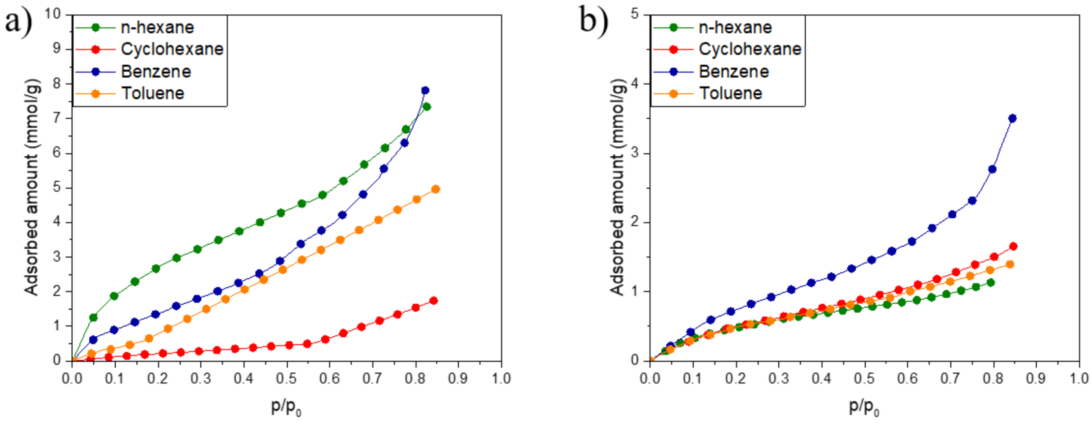

Figure 5. Experimental adsorption isotherms of selected VOCs for a) [Cu(2-pymo)$_2$]$_n$ and b) [Pd(2-pymo)$_2$]$_n$ at 25°C.

Computational study of the VOC adsorption

As described in the experimental part, GCMC simulations were carried out to investigate VOC adsorption within the MOF structures. Supercells were created from Crystallographic Information File (CIF) available in the Cambridge Crystallographic Data Center (CCDC) database. As evoked previously, [Cu(2-pymo)$_2$]$_n$ can adopt either cubic or rhombohedral structure depending on its exposure to the guest molecule (e.g. water). However, only the rhombohedral topology is observed once in direct contact with the studied series of VOCs. Hence, only this particular structure is exclusively taken into consideration for the simulations. The [Pd(2-pymo)$_2$]$_n$ structure keeps the same cubic topology whatever it is solvated or not. As we focused our utmost attention on benzene and n-hexane, the preferential location of these adsorbates was deduced for each MOF by injecting a single molecule into the supercell. GCMC simulations clearly show that benzene and n-hexane are not localized and distributed equally in both structures **(Figure 6)**.

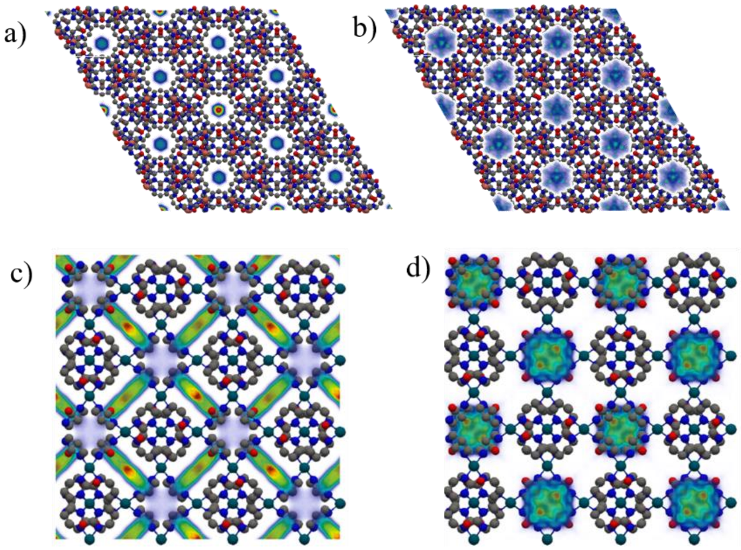

Figure 6. Density plots for a) n-hexane and b) benzene in [Cu(2-pymo)$_2$]$_n$. Density plots for c) n-hexane and d) benzene in [Pd(2-pymo)$_2$]$_n$.

The average occupation profiles of n-hexane and benzene reveal a preferential location within the hexagonal channels for [Cu(2-pymo)$_2$]$_n$, while the distribution pattern is more diversified in [Pd(2-pymo)$_2$]$_n$. Particularly, the benzene molecule seem to be preferentially located at the center of β cages, while the linear n-hexane crosses perpendicularly through the 6MR_H window connecting each cage. It is noteworthy that n-hexane does not pass through the 6MR_CO windows, probably because of their hydrophilicity.

Beyond the great value knowledge acquired on adsorption processes, information obtained from GCMC simulations also help to improve these MOFs through rational design for VOC capture purposes. Since steric effect prevents the penetration of toluene in the $[Pd(2\text{-pymo})_2]_n$ structure, a very precise increase of the ligand length may be a straightforward option if a capture of both benzene and toluene is required. On the other hand, the selectivity toward benzene could also be improved by further repelling other compounds such as n-hexane. As mentioned, n-hexane is only allowed to pass through 6MR_H due to its sufficient hydrophobicity (6MR_CO windows are forbidden). Moreover, replacing the _H group with hydrophilic functions such as carbonyl, hydroxyl or amine, should repel n-hexane and thus allow only benzene accommodation within the pores.

Conclusion

This study aims to explore the notorious affinity of aromatics to palladium based-materials and more specifically to MOFs with Pd nodes. In this respect, this work is a valuable contribution to the current state of the art through both experimental and simulation investigations of the aromatic VOCs sorption in a Pd-based MOF. Four VOCs (n-hexane, cyclohexane, benzene and toluene) were examined to assess the sorption properties of two isostructural MOFs: $[Cu(2\text{-pymo})_2]_n$ and $[Pd(2\text{-pymo})_2]_n$. QCM measurements showed that benzene exhibits higher affinity to Pd-based MOF while n-hexane has a preference for the Cu-based MOF. Toluene and cyclohexane are adsorbed in lower amounts due to their larger size and/or lower flexibility. GCMC simulations were useful to compare the localization of the adsorbed VOCs in both MOF structures. Benzene and n-hexane occupy hexagonal channels in $[Cu(2\text{-pymo})_2]_n$, while for $[Pd(2\text{-pymo})_2]_n$, benzene is localized in the β cages and n-hexane passes through the pore aperture perpendicularly to the 6MR-H. Attractively, the $[Pd(2\text{-pymo})_2]_n$ MOF clearly exhibits higher selectivity to benzene over other hydrocarbons, with a consistent adsorption capacity in comparison with the same volume of $[Cu(2\text{-pymo})_2]_n$. Overall, this study validates the highly favorable role of palladium as a metal node in MOF structure for the selective capture of aromatics. In addition, it also demonstrates that the involved charge interactions can be judiciously coupled with steric hindrance effects in the $[Pd(2\text{-pymo})_2]_n$ MOF network to favor the preferential capture and detection of benzene over toluene. This work paves the way to the design of high-performance materials for applications in specific aromatic adsorbing and/or sensing devices.

Associated Content

AUTHOR INFORMATION

Corresponding Author

* Martin Drobek - Institut Européen des Membranes, UMR 5635, Université de Montpellier, ENSCM, CNRS, Place Eugène Bataillon, F-34095 Montpellier cedex 5, France

Email: martin.drobek@umontpellier.fr

Authors

Kevin Dedecker - Institut Européen des Membranes (IEM); CNRS, ENSCM, Univ Montpellier; Place Eugène Bataillon; 34095 Montpellier; France

Email: kevin.dedecker@umontpellier.fr

Vincent Rouessac - Institut Européen des Membranes (IEM); CNRS, ENSCM, Univ Montpellier; Place Eugène Bataillon; 34095 Montpellier; France

Email: vincent.rouessac@umontpellier.fr

Anne Julbe - Institut Européen des Membranes (IEM); CNRS, ENSCM, Univ Montpellier; Place Eugène Bataillon; 34095 Montpellier; France

Email: anne.julbe@umontpellier.fr

Author Contributions

The manuscript was written through contributions of all authors. All authors have given approval to the final version of the manuscript.

Notes

The authors declare no competing financial interest. The funders had no role in the design of the study; in the collection, analyses, or interpretation of data; in the writing of the manuscript; or in the decision to publish the results.

Supporting Information

- PXRD patterns, IR spectra, TGA, N_2 adsorption-desorption measurements of $[Cu(2\text{-pymo})_2]_n$ and $[Pd(2\text{-pymo})_2]_n$, PXRD patterns of $[Cu(2\text{-pymo})_2]_n$ exposed to VOCs, computational details for GCMC simulations (PDF).

ACKNOWLEDGMENT

This research was funded in part by the ANR (SensMOFAir project #ANR-20-CE04-0012) and by the Région Occitanie in France (Défi clé Hydrogène Vert - Plan de relance - H2VERT- FEDER REACT EU - MOF-Hy sub-project). This project was also supported by Chimie Balard Cirimat Carnot Institute through the ANR program N°16 CARN 0008-01. The authors sincerely acknowledge Professor André Ayral (Institut Européen des Membranes) for his precious advices.

References

(1) Carslaw, N.; Creasey, D. J.; Harrison, D.; Heard, D. E.; Hunter, M. C.; Jacobs, P. J.; Jenkin, M. E.; Lee, J. D.; Lewis, A. C.; Pilling, M. J.; Saunders, S. M.; Seakins, P. W. OH and HO2 Radical Chemistry in a Forested Region of North-Western Greece. *Atmos. Environ.* **2001**, *35* (27), 4725–4737. https://doi.org/10.1016/S1352-2310(01)00089-9.

(2) Wang, Q.; Han, Z.; Wang, T.; Zhang, R. Impacts of Biogenic Emissions of VOC and NOx on Tropospheric Ozone during Summertime in Eastern China. *Sci. Total Environ.* **2008**, *395* (1), 41–49. https://doi.org/10.1016/j.scitotenv.2008.01.059.

(3) Carter, W. P. L. Development of Ozone Reactivity Scales for Volatile Organic Compounds. *J. Air Waste Manag. Assoc.* **1994**, *44* (7), 881–899. https://doi.org/10.1080/1073161x.1994.10467290.

(4) Li, A. J.; Pal, V. K.; Kannan, K. A Review of Environmental Occurrence, Toxicity, Biotransformation and Biomonitoring of Volatile Organic Compounds. *Environ. Chem. Ecotoxicol.* **2021**, *3*, 91–116. https://doi.org/10.1016/j.enceco.2021.01.001.

(5) Sharma, N.; Agarwal, A. K.; Eastwood, P.; Gupta, T. *Air Pollution and Control*, 1st ed.; Sharma, N., Agarwal, A. K., Eastwood, P., Gupta, T., Singh, A. P., Eds.; Energy, Environment, and Sustainability; Springer Singapore: Singapore, 2018. https://doi.org/10.1007/978-981-10-7185-0.

(6) Cheng, S.; Zhang, J.; Wang, Y.; Zhang, D.; Teng, G.; Chang-Chien, G. P.; Huang, Q.; Zhang, Y. B.; Yan, P. Global Research Trends in Health Effects of Volatile Organic Compounds during the Last 16 Years: A Bibliometric Analysis. *Aerosol Air Qual. Res.* **2019**, *19* (8), 1834–1843. https://doi.org/10.4209/aaqr.2019.06.0327.

(7) Montero-Montoya, R.; López-Vargas, R.; Arellano-Aguilar, O. Volatile Organic Compounds in Air: Sources, Distribution, Exposure and Associated Illnesses in Children. *Annals of Global Health*. Levy Library Press 2018, pp 225–238. https://doi.org/10.29024/aogh.910.

(8) Belingheri, M.; Fustinoni, S.; De Vito, G.; Porro, A.; Riva, M. A. Benzene and Leukemia: From Scientific Evidence to Regulations. A Historical Example. *Med. Lav.* **2019**, *110* (3), 234–240. https://doi.org/10.23749/mdl.v110i3.7995.

(9) Ifeanyi, O. E. A Review on Bezene and Haematological System. *Blood Res. Transfus. J.* **2018**, *2* (2), 1–5. https://doi.org/10.19080/OABTJ.2018.02.555582.

(10) Roma-Torres, J.; Teixeira, J. P.; Silva, S.; Laffon, B.; Cunha, L. M.; Méndez, J.; Mayan, O. Evaluation of Genotoxicity in a Group of Workers from a Petroleum Refinery Aromatics Plant. *Mutat. Res. - Genet. Toxicol. Environ. Mutagen.* **2006**, *604* (1–2), 19–27. https://doi.org/10.1016/j.mrgentox.2005.12.005.

(11) Cocheo, V.; Sacco, P.; Boaretto, C.; De Saeger, E.; Perez Ballesta, P.; Skov, H.; Goelen, E.; Gonzalez, N.; Baeza Caracena, A. Urban Benzene and Population Exposure. *Nature* **2000**, *404* (6774), 141–142. https://doi.org/10.1038/35004651.

(12) Dedecker, K.; Dumas, E.; Lavédrine, B.; Steunou, N.; Serre, C. 5 - Metal-Organic Frameworks for the Capture of Volatile Organic Compounds and Toxic Chemicals. In *Metal-Organic*

Frameworks (MOFs) for Environmental Applications; Elsevier, 2019; pp 141–178. https://doi.org/10.1016/B978-0-12-814633-0.00007-7.

(13) Shen, X.; Ou, R.; Lu, Y.; Yuan, A.; Liu, J.; Gu, J.; Hu, X.; Yang, Z.; Yang, F. Record-High Capture of Volatile Benzene and Toluene Enabled by Activator Implant-Optimized Banana Peel-Derived Engineering Carbonaceous Adsorbents. *Environ. Int.* **2020**, *143*, 105774. https://doi.org/10.1016/j.envint.2020.105774.

(14) Lu, W.; Wei, Z.; Gu, Z. Y.; Liu, T. F.; Park, J.; Park, J.; Tian, J.; Zhang, M.; Zhang, Q.; Gentle, T.; Bosch, M.; Zhou, H. C. Tuning the Structure and Function of Metal-Organic Frameworks via Linker Design. *Chem. Soc. Rev.* **2014**, *43* (16), 5561–5593. https://doi.org/10.1039/c4cs00003j.

(15) Liang, B.; Zhang, X.; Xie, Y.; Lin, R. B.; Krishna, R.; Cui, H.; Li, Z.; Shi, Y.; Wu, H.; Zhou, W.; Chen, B. An Ultramicroporous Metal-Organic Framework for High Sieving Separation of Propylene from Propane. *J. Am. Chem. Soc.* **2020**, *142* (41), 17795–17801. https://doi.org/10.1021/jacs.0c09466.

(16) Dedecker, K.; Pillai, R. S.; Nouar, F.; Pires, J.; Steunou, N.; Dumas, E.; Maurin, G.; Serre, C.; Pinto, M. L. Metal-Organic Frameworks for Cultural Heritage Preservation: The Case of Acetic Acid Removal. *ACS Appl. Mater. Interfaces* **2018**, *10* (16), 13886–13894. https://doi.org/10.1021/acsami.8b02930.

(17) Pires, J.; Fernandes, J.; Dedecker, K.; Gomes, J. R. B.; Pérez-Sánchez, G.; Nouar, F.; Serre, C.; Pinto, M. L. Enhancement of Ethane Selectivity in Ethane-Ethylene Mixtures by Perfluoro Groups in Zr-Based Metal-Organic Frameworks. *ACS Appl. Mater. Interfaces* **2019**, *11* (30), 27410–27421. https://doi.org/10.1021/acsami.9b07115.

(18) Van De Voorde, B.; Hezinová, M.; Lannoeye, J.; Vandekerkhove, A.; Marszalek, B.; Gil, B.; Beurroies, I.; Nachtigall, P.; De Vos, D. Adsorptive Desulfurization with CPO-27/MOF-74: An Experimental and Computational Investigation. *Phys. Chem. Chem. Phys.* **2015**, *17* (16), 10759–10766. https://doi.org/10.1039/c5cp01063b.

(19) Griessen, R.; Strohfeldt, N.; Giessen, H. Thermodynamics of the Hybrid Interaction of Hydrogen with Palladium Nanoparticles. *Nat. Mater.* **2016**, *15* (3), 311–317. https://doi.org/10.1038/nmat4480.

(20) Prentice, J. D.; Lesiunas, A.; Sheppard, N. Infrared Spectroscopic Evidence for π-Complex Formation from Ethylene Chemisorbed on Palladium and Platinum. *J. Chem. Soc. Chem. Commun.* **1976**, No. 2, 76–77. https://doi.org/10.1039/C39760000076.

(21) Greaves, E. O.; Lock, C. J. L.; Maitlis, P. M. Metal–Acetylene Complexes. II. Acetylene Complexes of Nickel, Palladium, and Platinum. *Can. J. Chem.* **1968**, *46* (24), 3879–3891. https://doi.org/10.1139/v68-641.

(22) Takahashi, A.; Yang, F. H.; Yang, R. T. Aromatics/Aliphatics Separation by Adsorption: New Sorbents for Selective Aromatics Adsorption by π-Complexation. *Ind. Eng. Chem. Res.* **2000**, *39* (10), 3856–3867. https://doi.org/10.1021/ie000376l.

(23) Luo, S.; Zeng, Z.; Zeng, G.; Liu, Z.; Xiao, R.; Chen, M.; Tang, L.; Tang, W.; Lai, C.; Cheng, M.; Shao, B.; Liang, Q.; Wang, H.; Jiang, D. Metal Organic Frameworks as Robust Host of Palladium Nanoparticles in Heterogeneous Catalysis: Synthesis, Application, and Prospect. *ACS Appl. Mater. Interfaces* **2019**, *11* (36), 32579–32598. https://doi.org/10.1021/acsami.9b11990.

(24) Szilágyi, P. A.; Callini, E.; Anastasopol, A.; Kwakernaak, C.; Sachdeva, S.; Van De Krol, R.; Geerlings, H.; Borgschulte, A.; Züttel, A.; Dam, B. Probing Hydrogen Spillover in Pd@MIL-101(Cr) with a Focus on Hydrogen Chemisorption. *Phys. Chem. Chem. Phys.* **2014**, *16* (12), 5803–5809. https://doi.org/10.1039/c3cp54898h.

(25) Liu, P.; Huang, Z.; Gao, X.; Hong, X.; Zhu, J.; Wang, G.; Wu, Y.; Zeng, J.; Zheng, X. Synergy between Palladium Single Atoms and Nanoparticles via Hydrogen Spillover for Enhancing CO2 Photoreduction to CH4. *Adv. Mater.* **2022**, *34* (16), 1–11. https://doi.org/10.1002/adma.202200057.

(26) Contescu, C. I.; Brown, C. M.; Liu, Y.; Bhat, V. V.; Gallego, N. C. Detection of Hydrogen

Spillover in Palladium-Modified Activated Carbon Fibers during Hydrogen Adsorption. *J. Phys. Chem. C* **2009**, *113* (14), 5886–5890. https://doi.org/10.1021/jp900121k.

(27) Weber, M.; Kim, J. H.; Lee, J. H.; Kim, J. Y.; Iatsunskyi, I.; Coy, E.; Drobek, M.; Julbe, A.; Bechelany, M.; Kim, S. S. High-Performance Nanowire Hydrogen Sensors by Exploiting the Synergistic Effect of Pd Nanoparticles and Metal-Organic Framework Membranes. *ACS Appl. Mater. Interfaces* **2018**, *10* (40), 34765–34773. https://doi.org/10.1021/acsami.8b12569.

(28) Qin, W.; Cao, W.; Liu, H.; Li, Z.; Li, Y. Metal-Organic Framework MIL-101 Doped with Palladium for Toluene Adsorption and Hydrogen Storage. *RSC Adv.* **2014**, *4* (5), 2414–2420. https://doi.org/10.1039/c3ra45983g.

(29) Parshamoni, S.; Nasani, R.; Paul, A.; Konar, S. Synthesis of a Palladium Based MOF: Via an Effective Post-Synthetic Modification Approach and Its Catalytic Activity towards Heck Type Coupling Reactions. *Inorg. Chem. Front.* **2021**, *8* (3), 693–699. https://doi.org/10.1039/d0qi01052a.

(30) Navarro, J. A. R.; Barea, E.; Salas, J. M.; Masciocchi, N.; Galli, S.; Sironi, A.; Ania, C. O.; Parra, J. B. Borderline Microporous-Ultramicroporous Palladium(Ii) Coordination Polymer Networks. Effect of Pore Functionalisation on Gas Adsorption Properties. *J. Mater. Chem.* **2007**, *17* (19), 1939–1946. https://doi.org/10.1039/b617698d.

(31) He, T.; Kong, X. J.; Zhou, J.; Zhao, C.; Wang, K.; Wu, X. Q.; Lv, X. L.; Si, G. R.; Li, J. R.; Nie, Z. R. A Practice of Reticular Chemistry: Construction of a Robust Mesoporous Palladium Metal-Organic Framework via Metal Metathesis. *J. Am. Chem. Soc.* **2021**, *143* (26), 9901–9911. https://doi.org/10.1021/jacs.1c04077.

(32) Navarro, J. A. R.; Barea, E.; Salas, J. M.; Masciocchi, N.; Galli, S.; Sironi, A.; Ania, C. O.; Parra, J. B. H2, N2, CO, and CO2 Sorption Properties of a Series of Robust Sodalite-Type Microporous Coordination Polymers. *Inorg. Chem.* **2006**, *45* (6), 2397–2399. https://doi.org/10.1021/ic060049r.

(33) Barea, E.; Navarro, J. A. R.; Salas, J. M.; Masciocchi, N.; Galli, S.; Sironi, A. Mineralomimetic Sodalite- and Muscovite-Type Coordination Frameworks. Dynamic Crystal-to-Crystal Interconversion Processes Sensitive to Ion Pair Recognition. *J. Am. Chem. Soc.* **2004**, *126* (10), 3014–3015. https://doi.org/10.1021/ja039472e.

(34) Rouessac, V.; van der Lee, A.; Bosc, F.; Durand, J.; Ayral, A. Three Characterization Techniques Coupled with Adsorption for Studying the Nanoporosity of Supported Films and Membranes. *Microporous Mesoporous Mater.* **2008**, *111* (1–3), 417–428. https://doi.org/10.1016/j.micromeso.2007.08.033.

(35) Sauerbrey, G. The Use of Quartz Oscillators for Weighing Thin Layers and for Microweighing. *Zeitschrift für Phys.* **1959**, *155* (2), 206–222. https://doi.org/10.1007/BF01337937.

(36) Dubbeldam, D.; Calero, S.; Ellis, D. E.; Snurr, R. Q. RASPA: Molecular Simulation Software for Adsorption and Diffusion in Flexible Nanoporous Materials. *Mol. Simul.* **2016**, *42* (2), 81–101. https://doi.org/10.1080/08927022.2015.1010082.

(37) Martin, M. G.; Siepmann, J. I. Transferable Potentials for Phase Equilibria. 1. United-Atom Description of n-Alkanes. *J. Phys. Chem. B* **1998**, *102* (14), 2569–2577. https://doi.org/10.1021/jp972543+.

(38) Keasler, S. J.; Charan, S. M.; Wick, C. D.; Economou, I. G.; Siepmann, J. I. Transferable Potentials for Phase Equilibria-United Atom Description of Five- and Six-Membered Cyclic Alkanes and Ethers. *J. Phys. Chem. B* **2012**, *116* (36), 11234–11246. https://doi.org/10.1021/jp302975c.

(39) Rai, N.; Siepmann, J. I. Transferable Potentials for Phase Equilibria. 9. Explicit Hydrogen Description of Benzene and Five-Membered and Six-Membered Heterocyclic Aromatic Compounds. *J. Phys. Chem. B* **2007**, *111* (36), 10790–10799. https://doi.org/10.1021/jp0735861.

(40) Rai, N.; Siepmann, J. I. Transferable Potentials for Phase Equilibria. 10. Explicit-Hydrogen Description of Substituted Benzenes and Polycyclic Aromatic Compounds. *J. Phys. Chem. B*

2013, *117* (1), 273–288. https://doi.org/10.1021/jp307328x.

(41) Rappé, A. K.; Casewit, C. J.; Colwell, K. S.; Goddard, W. A.; Skiff, W. M. UFF, a Full Periodic Table Force Field for Molecular Mechanics and Molecular Dynamics Simulations. *J. Am. Chem. Soc.* **1992**, *114* (25), 10024–10035. https://doi.org/10.1021/ja00051a040.

(42) Mayo, S. L.; Olafson, B. D.; Goddard, W. A. DREIDING: A Generic Force Field for Molecular Simulations. *J. Phys. Chem.* **1990**, *94* (26), 8897–8909. https://doi.org/10.1021/j100389a010.

(43) Lestari, W. W.; Adreane, M.; Purnawan, C.; Fansuri, H.; Widiastuti, N.; Rahardjo, S. B. Solvothermal and Electrochemical Synthetic Method of HKUST-1 and Its Methane Storage Capacity. *IOP Conf. Ser. Mater. Sci. Eng.* **2016**, *107* (1). https://doi.org/10.1088/1757-899X/107/1/012030.

(44) Chen, Y.; Mu, X.; Lester, E.; Wu, T. High Efficiency Synthesis of HKUST-1 under Mild Conditions with High BET Surface Area and CO2 Uptake Capacity. *Prog. Nat. Sci. Mater. Int.* **2018**, *28* (5), 584–589. https://doi.org/10.1016/j.pnsc.2018.08.002.

(45) Peralta, D.; Chaplais, G.; Simon-Masseron, A.; Barthelet, K.; Chizallet, C.; Quoineaud, A. A.; Pirngruber, G. D. Comparison of the Behavior of Metal-Organic Frameworks and Zeolites for Hydrocarbon Separations. *J. Am. Chem. Soc.* **2012**, *134* (19), 8115–8126. https://doi.org/10.1021/ja211864w.

(46) Headen, T. F.; Howard, C. A.; Skipper, N. T.; Wilkinson, M. A.; Bowron, D. T.; Soper, A. K. Structure of π-π Interactions in Aromatic Liquids. *J. Am. Chem. Soc.* **2010**, *132* (16), 5735–5742. https://doi.org/10.1021/ja909084e.

(47) Chipot, C.; Jaffe, R.; Maigret, B.; Pearlman, D. A.; Kollman, P. A. Benzene Dimer: A Good Model for π-π Interactions in Proteins? A Comparison between the Benzene and the Toluene Dimers in the Gas Phase and in an Aqueous Solution. *J. Am. Chem. Soc.* **1996**, *118* (19), 11217–11224. https://doi.org/10.1021/ja961379l.

(48) Law, K. S.; Schauer, M.; Bernstein, E. R. Dimers of Aromatic Molecules: (Benzene)2,

(Toluene)2, and Benzene-Toluene. *J. Chem. Phys.* **1984**, *81* (11), 4871–4882. https://doi.org/10.1063/1.447514.

TOC